

Comparative Analysis of Metallic Nanoparticles as Exogenous Soft Tissue Contrast for Live In Vivo Micro-Computed Tomography Imaging of Avian Embryonic Morphogenesis

Chelsea L. Gregg and Jonathan T. Butcher *

Meinig School of Biomedical Engineering, Cornell University, Ithaca, New York

Background: Gestationally survivable congenital malformations arise during mid–late stages of development that are inaccessible in vivo with traditional optical imaging for assessing long-term abnormal patterning. MicroCT is an attractive technology to rapidly and inexpensively generate quantitative three-dimensional (3D) datasets but requires exogenous contrast media. Here we establish dose-dependent toxicity, persistence, and biodistribution of three different metallic nanoparticles in day 4 chick embryos. **Results:** We determined that 110-nm alkaline earth metal particles were nontoxic and persisted in the chick embryo for up to 24 hr postinjection with contrast enhancement levels at high as 1,600 Hounsfield units (HU). The 15-nm gold nanoparticles persisted with x-ray attenuation higher than that of the surrounding yolk and albumen for up to 8 hr postinjection, while 1.9-nm particles resulted in lethality by 8 hr. We identified spatial and temporally heterogeneous contrast enhancement ranging from 250 to 1,600 HU. With the most optimal 110-nm alkaline earth metal particles, we quantified an exponential increase in the tissue perfusion vs. distance from the dorsal aorta into the flank over 8 hr with a peak perfusion rate of $0.7 \mu\text{m}^2/\text{s}$ measured at a distance of 0.3 mm. **Conclusions:** These results demonstrate the safety, efficacy, and opportunity of nanoparticle based contrast media in live embryos for quantitative analysis of embryogenesis. *Developmental Dynamics* 245:1001–1010, 2016. © 2016 Wiley Periodicals, Inc.

Key words: embryo; development; nanoparticles; toxicity; biodistribution; dorsal aorta; perfusion

Submitted 29 January 2016; First Decision 7 June 2016; Accepted 14 June 2016; Published online 22 July 2016

Introduction

Embryonic development is a rapid and dynamic three-dimensional (3D) process characterized by the growth and differentiation of progenitor cell populations into a complex network of organs and supporting tissues. Although much has been learned about the gross anatomical changes that occur during morphogenesis, elucidating the mechanistic interplays between underlying biomechanical and biochemical cues is critical for integrating the genetic and environmental influences on tissue behavior. Outside of the earliest stages of development, our understanding of this highly dynamic process has been gleaned primarily from static reconstructions of animal models. This gap obscures our knowledge of relative growth rates, prioritization, and distinction between association and causality. Genetic mutations that alter early stage patterning are nearly always

embryonic lethal, but gestationally survivable malformations arise during the mid–late stages of development after initial fate specification and tissue patterning have begun (Roger et al., 2010). Propagation of even subtle abnormalities at these stages can lead to congenital defects with a range of severities, origins that are largely unknown, and potentially bleak prognoses (Gregg and Butcher, 2013).

High-resolution, quantitative dynamic imaging technologies are, therefore, essential for capturing these emerging knowledge needs in embryonic development. Although high-resolution 3D reconstructions from histological sections are commonplace, these are static representations of postvital organisms. Optical resolution is unparalleled within the sectioning plane but out of plane 3D interpolation between multiple sections is time consuming and suffers from inherent error in embedding and sectioning.

The vast majority of live embryonic inquiry has focused on the early events of development spanning gastrulation and heart tube formation with the onset of beating (Czirók et al., 2004; Zamir et al., 2006; Cui et al., 2013). Confocal and multiphoton microscopy with excitable and infrared fluorophores is capable of

Additional supporting information may be found in the online version of this article

Grant sponsor: the National Heart, Lung, and Blood Institute; Grant number: #HL110328; Grant number: HL128745; Grant sponsor: the National Science Foundation; Grant number: CBET-0955172.

*Correspondence to: Jonathan T. Butcher, Nancy E. and Peter C. Meinig School of Biomedical Engineering, 304 Weill Hall, Cornell University, Ithaca NY 14853. E-mail: alansmith@unj.edu

Article is online at: <http://onlinelibrary.wiley.com/doi/10.1002/dvdy.24433/abstract>
© 2016 Wiley Periodicals, Inc.

imaging up to 2 mm in live samples (Squirrell et al., 1999; Dickinson et al., 2003; Supatto et al., 2005, 2009; Diaspro et al., 2005) with limited capacity once the tissue becomes dense and light scattering beyond the earliest stages of development. Live embryonic studies conducted during mid-late stages of development are more limited, requiring a reliable animal model and high-resolution, wide field, deep tissue imaging.

Live in vivo imaging with ultrasound and MRI often suffer from restrictions in field of view, signal-to-noise ratio, and differential tissue contrast (Metscher, 2009). Ultrasound is widely used for screening hemodynamic profiles in developing embryos and couples nicely with 3D reconstructions for further computation analysis of fluid-solid tissue interactions (Wessels and Sedmera, 2003; Yu et al., 2004; Shen et al., 2005; Yu et al., 2015). Whole specimen MRI studies are emerging as radio frequency coil design and postprocessing techniques improve, but MRI remains an expensive and a lengthy scanning process (especially for very high resolutions) requiring additional considerations for environmental control to maintain healthy, viable samples (Gregg and Butcher, 2012). Micro-computed tomography (microCT) is an attractive three dimensional whole specimen imaging technology for morphogenetic inquiry having the resolution and depth of field required to capture mid-late stages of embryonic development with high fidelity at a fraction of the cost of MRI (Gregg and Butcher, 2012).

MicroCT has been a valuable imaging tool for the past 15 years in the field of embryological research characterizing tortuous anatomy with high spatial and temporal resolution (Butcher et al., 2007). MicroCT imaging produces high-resolution 3D datasets within minutes at a fraction of the cost of similar technologies (Kim et al., 2011). Advancements in CT dense contrast media and sophisticated protocols enable high tissue boundary identification with general and molecularly targeted exogenous soft tissue contrast (Butcher et al., 2007; Metscher, 2009; Metscher and Müller, 2011; Yalcin et al., 2011; Gregg et al., 2015). MicroCT imaging can readily identify multiple and broad 3D morphological consequences of transgenic modifications on fixed developing embryos (Johnson et al., 2006; Degenhardt et al., 2010).

Furthermore, whole-mount staining with antibody probes and metal immunodetection has yielded tissue patterning data in the developing chick embryo (Metscher & Müller, 2011; Gregg et al., 2015). Coupled 3D microCT anatomical data with Doppler ultrasound has shown to be a power tool for computational analysis of hemodynamic patterning in the developing chick heart (Yalcin et al., 2011). While microCT has served a much needed purpose for high-resolution, deep tissue imaging of embryos, the inability to gather longitudinal (time course) data from the same embryo necessitates the preparation of multiple samples for single time points, increasing experimental variability particularly if genetic perturbations or microsurgical manipulations are present. It is essential to extend microCT imaging to live samples to address these limitations.

We previously established the possibility for nontoxic live microCT imaging using VisipaqueTM (VP) in an avian embryo model (Henning et al., 2011). We showed that radiation from scans up to $7 \times$ higher than typical scan dosage did not cause morphological defects for embryos up to day 10 of development. Iodine based molecules, such as VP, have been the standard contrast media for x-ray and CT images proving themselves safe and effective (Scheller et al., 1999). Such free molecule contrast media are < 1 nm, and, therefore, extravasate quickly with dramatic

reduction in contrast after a few hours, too short for meaningful longitudinal analysis from a single injection. Injectable nanoparticle technology has achieved long residence times and high levels of x-ray attenuation, motivating their potential as embryonic imaging contrast (Boll et al., 2011; Nebuloni et al., 2013; Lee et al., 2014; Ashton et al., 2014). Nanoparticles, which can be fabricated out of multiple materials (e.g., gold, earth metals, tungsten, liposomes encapsulating VP), have been used extensively in cancer research as an imaging and delivery tool (Melancon et al., 2014; Zarschler et al., 2014).

Additionally, biomolecule conjugation to the nanoparticle surface enables targeting of different tissue types (Wen et al., 2001; Melancon et al., 2014). Nanoparticle based CT contrast media have not been extended to live embryonic imaging to date. In this study, we address longitudinal use of nanoparticle based exogenous soft tissue contrast for live microCT imaging of embryonic development in the avian embryo. Intravenous delivery and toxicity of three different metallic nanoparticles were assessed. Furthermore, we analyzed particle material and size contributions on spatial and temporal contrast enhancement of day 4–5 embryos. Lastly, we quantified relative perfusion characteristics by means of bulk particle movements in embryonic tissue.

We demonstrate that alkaline earth 110-nm metallic nanoparticles are more radiopaque within the embryo than their 15-nm and 1.9-nm gold nanoparticle counterparts. Additionally, we found that the 110-nm particles persist longest in the embryo and yields high tissue boundary delineation with time dependent and organ dependent contrast enhancement. The 15-nm gold nanoparticles persisted for at least 8 hr postinjection and the 1.9-nm gold nanoparticles extravasated quickly out of the vasculature into the embryonic tissue and were toxic to the embryo by 8 hr postinjection. Lastly, we quantified relative perfusion of the 110-nm alkaline earth metal particles moving out of the dorsal aorta into the surrounding tissue based on transient contrast enhancement changes.

Results

Temporal Nanoparticle Toxicity and X-ray Attenuation During In Vivo MicroCT Imaging

Acute and long-term toxicity from metallic nanoparticle exposure were assessed using heart rate and anatomical analysis, respectively. Embryonic heart rate was recorded immediately before (0-), immediately after (0+), 1 hr, and 24 hr postinjection (Fig. 1A). Exposure to the microinjection procedure caused a significant but transient drop in heart rate from baseline preinjections levels in 15-nm AuNPs from 143 bpm to 104 bpm, in 110-nm EXTNs from 161 bpm to 111 bpm, and in Earl's balanced salt solution (EBSS) from 147 bpm to 109 bpm in injected samples (Fig. 1A). All heart rates recovered within 1 hr postinjection with no significant difference between the 0-preinjection levels for each respective injected media and between different types of media. This small transient dip is consistent with previous observations from nearly identical experimental procedures resulting in no long-term, deleterious consequences to the samples (Henning et al., 2011).

All samples injected with the 1.9-nm AuNP particles died within 8 hr postinjection. The concentration of metallic gold material in the 1.9-nm AuNP is identical to the 15-nm AuNP particles,

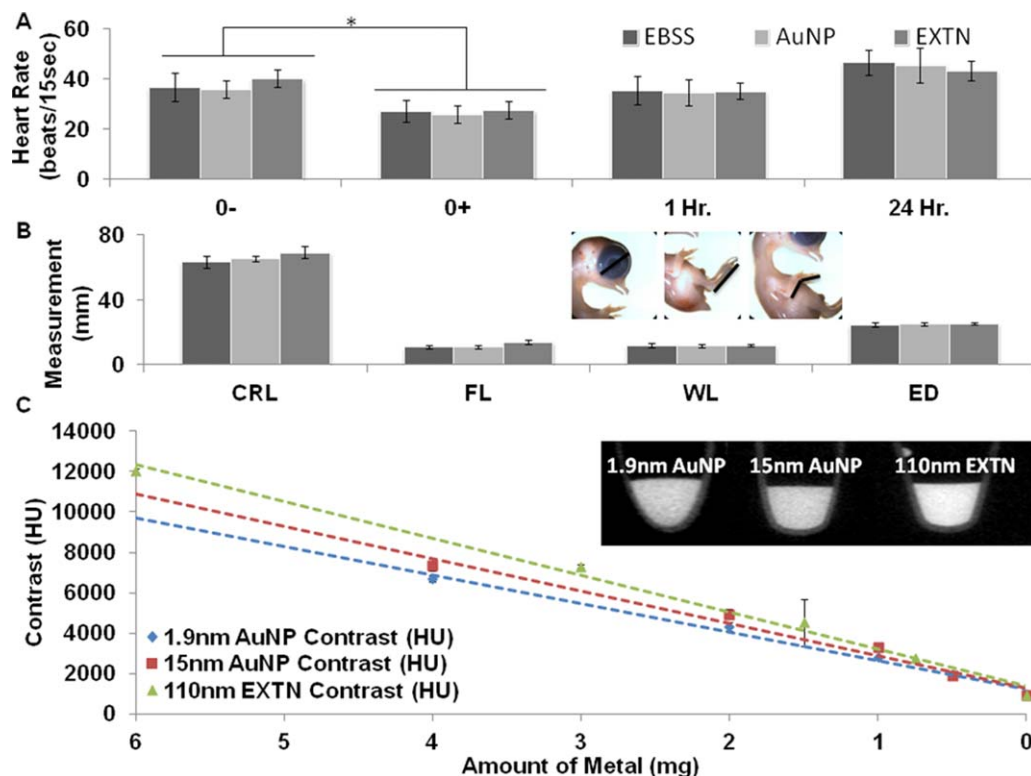


Fig. 1. **A:** Acute heart rate analysis of day 3 chicks following treatment with metallic nanoparticle contrast media injected at 10% blood volume with EBSS serving as a negative control. A significant heart rate decline was observed immediately postinjection (0+) across all contrast medias and EBSS controls ($P < 0.05$) but heart rates returned to their initial values within 1 hr postinjection ($n = 10, 10, 4$). **B:** Anatomical analysis one week post exposure to metallic nanoparticle contrast media (day 10 embryos) reveals no morphological defects for either the 15-nm AuNP or the 110-nm EXTN particles when compared with EBSS controls ($P < 0.05$; $n = 9, 9, 4$). **C:** Modeled particle contrast degradation vs. to the amount of metal (mg) present in the solution determined through a dilution series ranging from 100% particle solution to 0% ($1 \times$ PBS) with inset representative media diluted at 12.5% concentration from the stock solution ($n = 3$).

with the only difference being the size of particles themselves, indicating that toxicity is not only dose dependent but also size dependent of the particle (Pan et al., 2009). With the exception of embryos injected with the 1.9-nm AuNP particles, viability of embryos injected with either the 15-nm AuNP or the 110-nm EXTN nanoparticles was no different than that of controls. We next analyzed resulting embryonic morphology through anatomical measurements of day 10 embryos to see if particles induced malformations during development. No gross anatomical malformations were observed between samples injected with particles as compared to EBSS control (Fig. 1B). The wing length (WL), foot length (FL), eye diameter (ED), and total crown-rump length (CRL) were consistent with no statistically significant differences between the samples injected with 15-nm AuNPs or 110-nm EXTNs as compared to measurements obtained from the EBSS controls suggesting that development proceeded normally in all nanoparticle exposed embryos. Subsequent scans on Day 10 embryos that were injected at Day 4 were inspected for gross internal organ malformations (e.g., heart, eye, brain, liver size/shape/positions), of which none were found. This was consistent with our previous contrast injection study (Henning et al., 2011).

As expected, we identified a linear reduction of x-ray attenuation with contrast dilution for all particle types considered (Fig. 1C). The amount of metal was extrapolated from known metal concentrations in all particle stock solutions. The upper limit of contrast enhancement achieved for each particle type at a 10%

injection volume is 1,800 Hounsfield units (HU), 1,940 HU, and 2,500 HU for the 1.9-nm AuNP, 15-nm AuNP, and 110-nm EXTN, respectively.

Comparison of Local Contrast Enhancement Between Particle Types

Comparison of spatial particle distribution demonstrates greater heterogeneity with the 110-nm EXTN particles as compared to the smaller 1.9-nm and 15-nm AuNP particles. Structures associated with the vascular system, particularly the heart, dorsal aorta, and extraembryonic vasculature were visualized immediately postinjection with representative images being taken within the first 30 min postinjection (Fig. 2B). Contrast enhancement was measured in the heart, dorsal aorta, head measured at the mesencephalon, limb, and allantoic sac immediately postinjection (Fig. 2A). The contrast enhancement produced by the 110-nm EXTN particles was significantly higher in the heart, dorsal aorta, and limb with levels as high as 1,560 HU immediately postinjection ($P < 0.05$). Contrast enhancement was the same in the head and allantois between all particle types considered with no significant differences measured immediately postinjection (Fig. 2A). Visualization of sagittal image sections in representative embryos (Fig. 2B) demonstrates qualitative spatial contrast enhancement differences within the same embryo and across particle types. The 1.9-nm particles quickly extravasate from the vasculature and

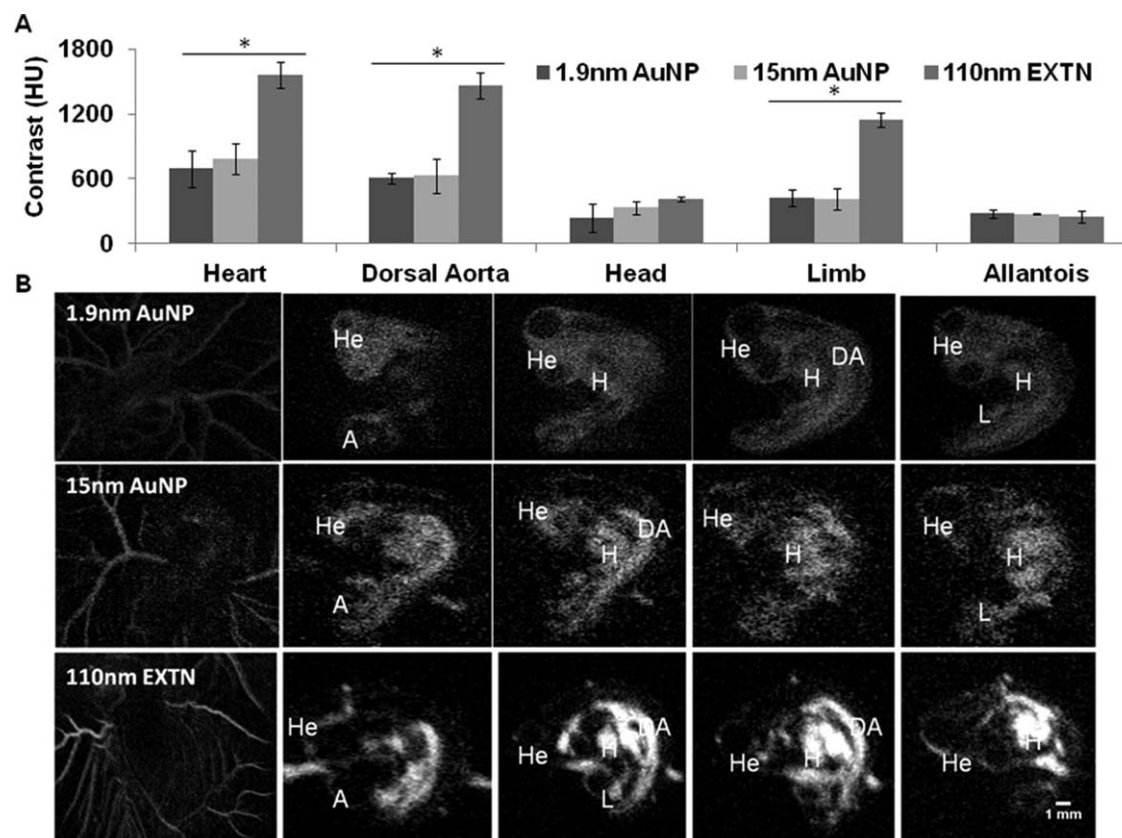


Fig. 2. **A:** Comparison of peak contrast enhancement between three different metallic nanoparticle contrast media microinjected into day 4 chick embryos at 10% blood volume. Contrast enhancement was measured within the heart, dorsal aorta, head, limb, and allantoic sac ($n = 3$). Contrast was significantly higher in embryos treated with 110-nm EXTN particles ($P < 0.05$) for the heart, dorsal aorta, and limb. **B:** Representative 2D gray-scale cross-section images through the sagittal plane labeled with developing organ systems of day 4 chick embryos. The 110-nm EXTN particles demonstrate higher x-ray attenuation and soft tissue contrast enhancement as compared to the gold nanoparticles. Furthermore, a size dependent extravasation is suggested due to larger particles retained in the vasculature whereas the smallest 1.9-nm AuNP particles have extravasated into the surrounding tissue. H, heart; He, head; DA, dorsal aorta; L, limb; and A, allantois.

luminal spaces into the surrounding tissue, an observation not comparatively seen with the 110-nm EXTN particles suggesting a size specific component to particle perfusion into the tissue.

The 3D renderings show maximum intensity and volumetric information of the embryo and surrounding extra embryonic vasculature (Fig. 3). Maximum intensity projections (MIPs) were generated and mapped to the same color intensity legend (Fig. 3A) between all particle types allowing direct comparison of spatial contrast intensity revealing particle locations and their relative concentrations. The 1.9-nm AuNP MIP rendering has homogeneous particle distribution within the embryo with no clear concentrations throughout the volume suggesting fast extravasation and distribution of particles through the tissue (Fig. 3A). 3D analysis of embryos injected with the 15-nm AuNPs reveals minimal concentration of the particles within the heart and dorsal aorta that is most proximal to the heart indicated through the color map (Fig. 3A). These results are also consistent with the measured contrast values (Fig. 2A) with highest enhancement found in the cardiovascular system. The largest heterogeneity of spatial particle contrast enhancement is visualized with the 110-nm EXTN particles (Fig. 3A). High enhancement is observed in the heart, dorsal aorta, and vitelline vascular network denoted by the shift in the color map, whereas the head and allantois have minimal particle concentration (Fig. 3A; Supplementary Movie, which is

available online). Volumetric renderings (VRs) reveal all density information of the embryo (Fig. 3B). Subtleties of soft tissues around highly vascularized tissues are revealed in more detail, particularly soft tissues surrounding the dorsal aorta and somites on the dorsal side of the embryo (Fig. 3B) best seen with the 110-nm EXTN particles.

Temporally Changing Organ Specific Contrast Enhancement

Contrast persistence and distribution was monitored for up to 24 hr postinjection. The 1.9-nm AuNP embryos did not survive to the 8- to 9-hr time point, but the 15-nm AuNP and 110-nm EXTN embryos survived for 24 hr postinjection for a total of three imaging time points. Heterogeneous spatial contrast enhancement was observed in all three particle types immediately postinjection with the highest contrast enhancement associated with the cardiovascular system (Fig. 4A–C). Over a 24-hr period of time, contrast enhancement degraded in both 15-nm AuNP and 110-nm EXTN particles in the heart, dorsal aorta, limb, and head. At 8 hr postinjection with the 15-nm AuNPs, all organs considered were statistically the same with contrast levels ranging from 160–250 HU (Fig. 4B). However, the 110-nm EXTN particles at 8 hr postinjection had statistically similar contrast enhancement

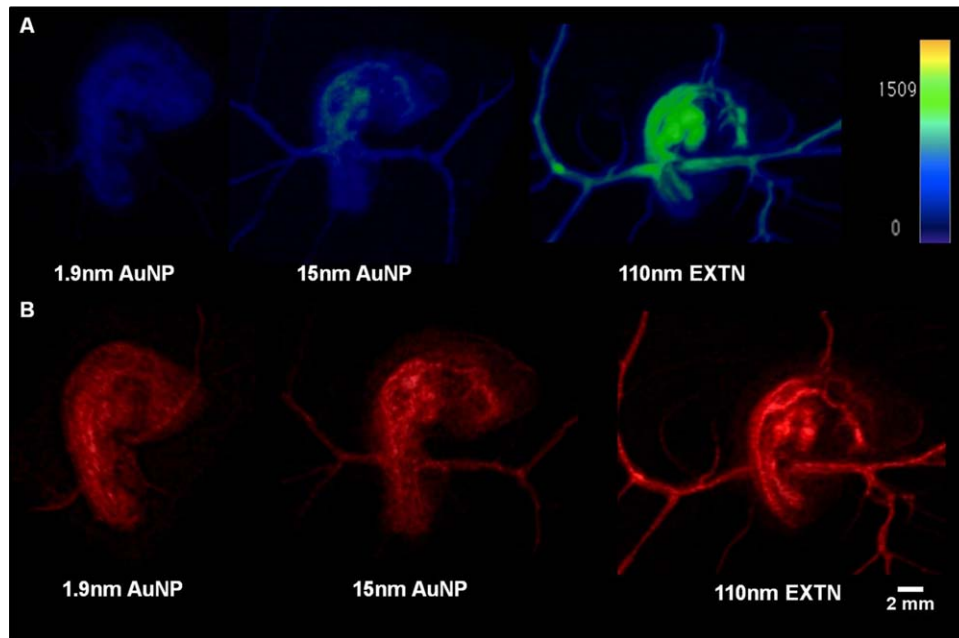


Fig. 3. Representative 3D renderings of day 4 chick embryos microinjected with different metallic nanoparticle contrast media and imaged at 50- μ m resolution with 800 projection scans. **A:** MIPs of day 4 chicks calibrated to a single contrast enhancement color map given in the image denoting localized higher and lower contrast values measured in HU. **B:** VRs of day 4 chicks injected with different contrast media. Also see the Supplementary Movie (3D MIP).

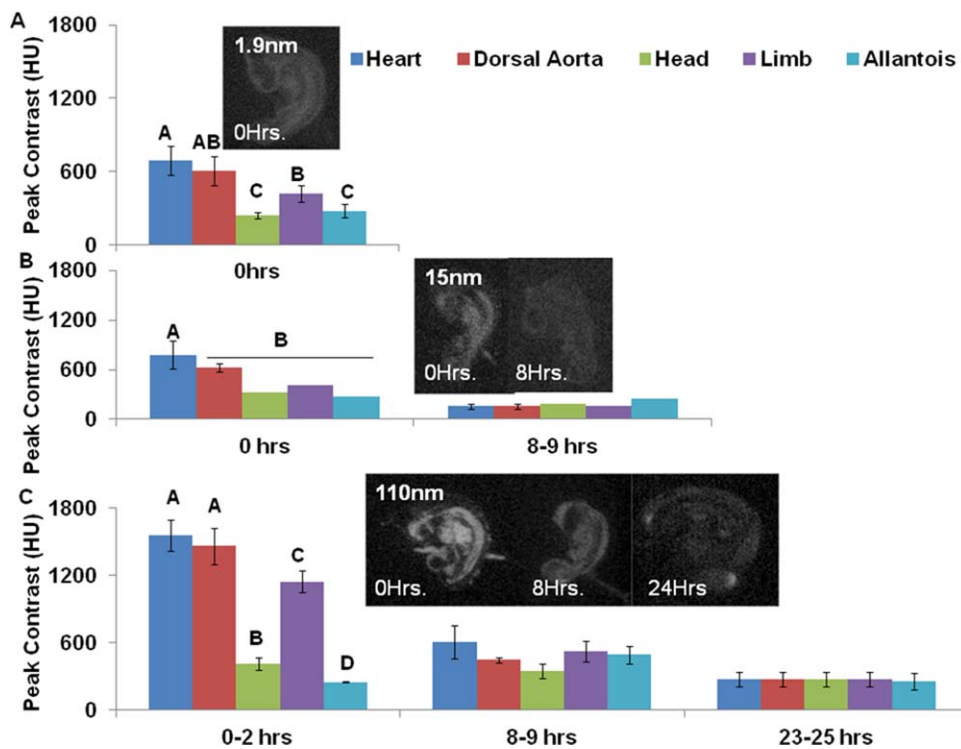


Fig. 4. Temporal contrast enhancement comparison. **A:** Contrast enhancement of the 1.9-nm AuNP particles across multiple organ systems. Contrast extravasated quickly from the vasculature into the surround tissue and all samples died within 8 hr postinjection. **B:** Contrast enhancement of the 15-nm AuNP particles over 8 hr postinjection. Cardiovascular structures were visualized readily immediately postinjection and by 8 hr contrast enhancement was the same across the embryo. Embryos survived for 24 hr postinjection but contrast enhancement at 24 hr was not different from the background resulting in zero visualization of the embryo. **C:** Contrast enhancement in day 4 embryos treated with 110-nm EXTN particles produced the highest levels of contrast with strong attenuation in structures with high vascularity but enhancement across the embryo equalized by 8 hr postinjection but tissue boundaries were still readily visualized. At 24 hr postinjection, tissue boundaries were not readily seen but the embryonic body was visualized as compared to background.

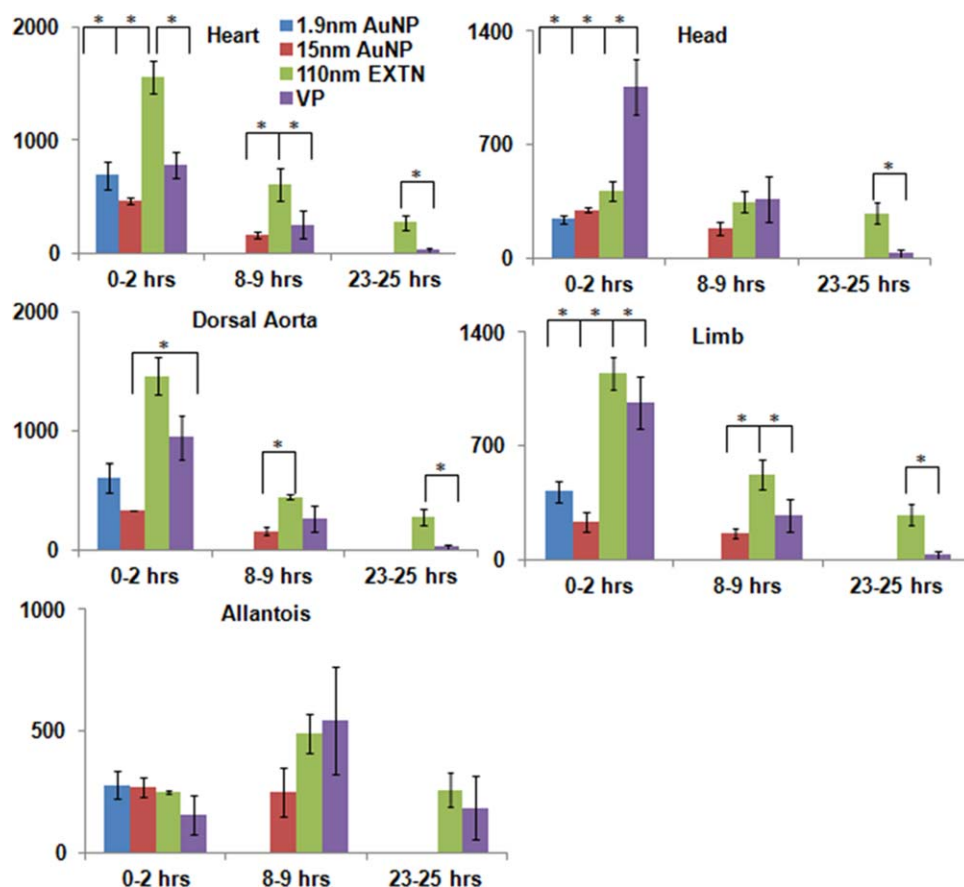


Fig. 5. Direct metallic nanoparticle comparison as compared to Visipaque. Contrast enhancement in each organ system considered for this study was compared across all three particles types presented against the previously published VP. The 110-nm EXTN particles outperformed VP particularly in the cardiovascular structures, maintaining significantly high attenuation at 8 hr postinjection in the hearts, dorsal aorta, and limb. At 24 hr postinjection, the 110-nm EXTN particles outperformed the VP demonstrating high levels of contrast enhancement in the embryonic body.

in all organs but the overall contrast intensity was higher than that of the 15-nm AuNPs with levels ranging from 350–600 HU (Fig. 4C).

At 24 hr postinjection, contrast enhancement in the 15-nm AuNP embryos was not distinguishable from background noise suggesting that the particles had extravasated out of the embryonic body into the extra embryonic space with homogenous distribution between the embryo and the albumen. At 24 hr postinjection, contrast enhancement of 110-nm EXTN embryos was nearly identical in all organs considered with an average value of 272 ± 7 HU; Fig. 4C). Specific tissue delineation in the 24 hr 110-nm EXTN embryos was not readily visualized given the equal distribution of the particles within all tissues but the overall embryonic body was seen as compared to the background.

Comparison to previously published VP data (Henning et al., 2011) reveals that the 110-nm EXTN particles outperform all other nanoparticle types and VP. The heart and dorsal aorta have significantly higher contrast enhancement in the 110-nm EXTN embryos vs. the VP embryos with values of 1,557 HU and 1,462 HU for 110-nm EXTN and 786 HU and 945 HU for VP in the heart and dorsal aorta, respectively, immediately postinjection (Fig. 5). Furthermore, analysis 24 hr later reveals persistence of the 110-nm EXTN levels significantly higher than all organs considered except the allantois than the VP (Fig. 5).

Modeled Particle Perfusion From the Dorsal Aorta Into the Surrounding Tissue

Nanoparticles perfuse across the endothelium of the vasculature into the surrounding tissue of the embryonic body before perfusing into the remaining extra-embryonic space. Unique to the 110-nm EXTN particles, perfusion of the particles from the vascular system into the surrounding tissue can be quantified within the first 8 hr postinjection where tissue boundaries are still visualized, enabling quantification of particle movement rates out of major vascular structures. Contrast enhancement per amount of metal is known from the dilution data previously given (Fig. 1C) and the stock solution of the EXTN particles is 300 mg/ml of metal. We chose to quantify perfusion from the dorsal aorta into the flank mesenchyme. The perfusion coefficient vs. distance (Fig. 6A) increases exponentially with increasing distance from the dorsal aorta. A faster rate of perfusion farther from the dorsal aorta is correlative to lower contrast enhancement away from the dorsal aorta (Fig. 6B).

Measured perfusion rates ranged from $0.06 \mu\text{m}^2/\text{s}$ to $0.7 \mu\text{m}^2/\text{s}$ for distances ranging from 0.1 to 0.3 mm, respectively. MIP 3D reconstructions reveal overall contrast enhancement based on a controlled color map (Fig. 6B) at the two time points considered. Inset images, magnified to the same portion of the dorsal aorta, reveal changes in contrast enhancement over an 8-hr period.

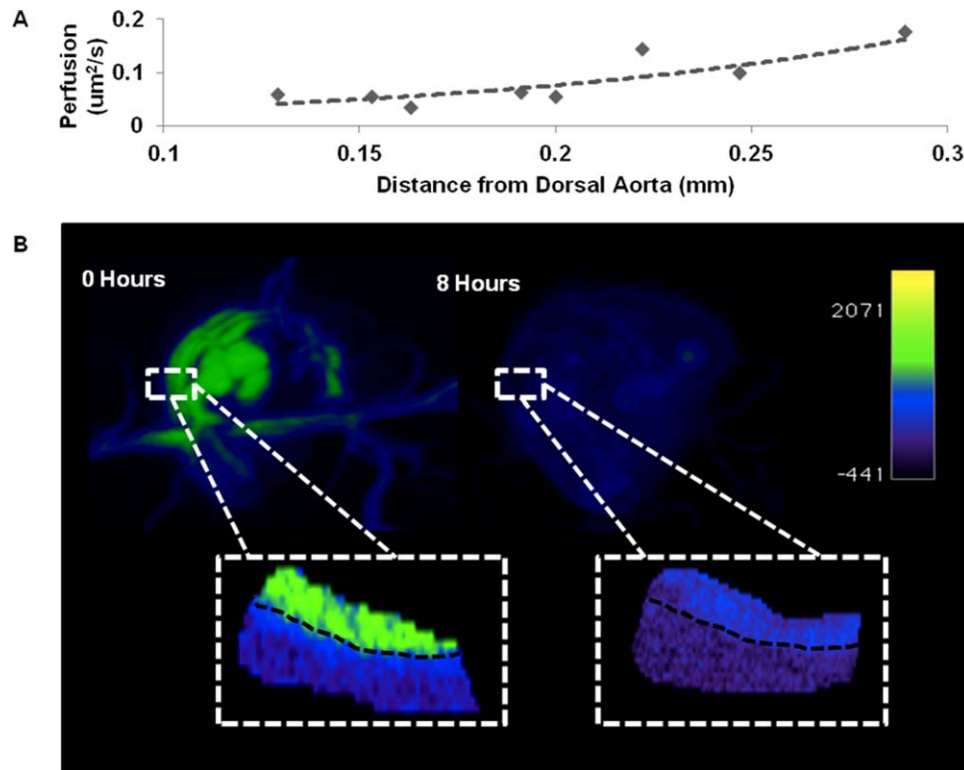


Fig. 6. **A:** Modeled particle diffusion over an 8-hr period of time from the dorsal aorta, sampled above the vitelline vein. Contrast enhancement was measured at known distances away from the dorsal aorta at 8 hr postinjection. Concentration and amount of metal values were derived from standard curves previously established (Fig. 1). Fick's first law of diffusion was used to interpolate the diffusion coefficient as a function of distance from the dorsal aorta 8 hr postinjection. **B:** Representative MIPS of immediately postinjection (0 hr) and 8 hr postinjection chick embryos with magnified insets of the dorsal aorta (black dashed line) and surrounding tissue. Color map based on contrast enhancement (HU) given in the legend.

These images reveal a significant decrease in contrast enhancement within the dorsal aorta and decreasing contrast enhancement as distance increases away from the dorsal aorta indicating the increasing rate of perfusion with distance (Fig. 6).

Discussion

We demonstrate that nanoparticle based contrast enhancement is safe and effective for live in vivo microCT imaging of embryonic development. We show that the 110-nm EXTN particles surpass the gold nanoparticles in contrast enhancement, residence time, and identifiable tissue boundaries. Furthermore, we show that contrast enhancement of the embryo remains at high levels 24 hr postinjection than the previously published VP. The best images of the cardiovascular structures was seen immediately postinjection, whereas the best analysis of the allantois is 8 hr postinjection when contrast has reached its peak. Furthermore, our data suggest alternate clearance mechanisms than that observed with the VP studies, indicating extravasation of particles into the tissue where it further moves down a concentration gradient out of the embryonic body. Additionally, particles may also be transported into the cell by means of endocytosis, a mechanism that is out of the scope of this study but indicates future experimental opportunities. Given the increased time in reliable tissue boundary recognition, quantitative analysis into transport processes is possible. Here, we present a method for characterizing relative perfusion coefficients from the dorsal aorta into the surround

tissue, demonstrating the ability for powerful insights into passive and active transport phenomena within live embryos.

MicroCT is a promising tool in 3D embryonic imaging for mid-late stage in vivo studies fulfilling the needed resolution and depth of field required for capturing these stages of development (Gregg and Butcher, 2012). Previous studies established the dose-dependent toxicity of x-ray radiation on avian embryos (Henning et al., 2011), determining that a radiation dose of 798 mGy would be required to induce morphological defects within the time period being considered, a level far above what is required for microCT imaging and what was presented in this study. The most pressing challenge associated with live imaging of embryos using microCT is the lack of available nontoxic, nonteratogenic contrast media. Several exogenous soft tissue contrast agents have been used in embryonic imaging (Butcher et al., 2007) but nearly all contrast media has proven to be lethal. A detailed explanation of all contrast media, excluding the media used in this study, has been given in previous literature (Gregg et al., 2015).

Before this study, the only nontoxic contrast media for live embryonic microCT imaging to our knowledge was VP (Henning et al., 2011) becoming the standard of comparison for live embryonic microCT imaging. In this study, the 110-nm EXTN particles outperformed all other contrast media, including VP. EXTN particles remained in the vasculature the longest with enhancement remaining up to 8 hr postinjection. After 24 hr postinjection, while vascular contrast was not distinguishable from the embryonic tissue, contrast enhancement remained within the embryonic body. Differences between nanoparticles in rates of extravasation and

clearance from the embryo proper suggest a size dependent mechanism. For the metallic particles to extravasate into the surrounding embryonic tissue, they must cross the endothelium. The primitive vasculature is active and present throughout the time period of the presented study (days 4–5), but the blood vessels are immature in structure and function.

Basic vascular architecture arises in the earliest stages of development before blood flow initiation (Sabin, 1917). Fusion and transformation of endothelial and angioblast progenitor cells into lamina produce the primitive vascular networks (vasculogenesis), from which sprouting and capillary formation occurs (angiogenesis). Primary blood vessels undergo much remodeling to eventually form the mature vascular system at the end of development (Risau and Flamme, 1995). A vast majority of vessels that arise throughout development regress, serving functions only for the development of a variety of different organ systems such as capillaries found in the prechongrogenic areas of the embryo (Risau and Flamme, 1995). Continuous sprouting and regression of blood vessels results in an immature endothelium during much of development. Endothelial lamina and other structural component (organelles, junction components) are found in the chick embryo vessels by day 4 of development (Roy et al., 1974) but basement membrane structure is ill formed until day 18 of chick development and the tight junction complexes are “leaky” until the latest stages of development (Roy et al., 1974), indicating that extravasation of molecules, and in the case of this study, particles will readily occur across the endothelium.

Without a developed renal system, primitive filtering in embryos at the stages considered is in part attributed to the allantois. In early mid stage embryos (days 4–5), the allantois serves to store and excrete nitrogenous metabolites from the embryo (Bellairs and Osmond, 2014) with increasing ability of active transport across the allantoic epithelium (Graves et al., 1986). Henning et al. found that VP was readily filtered into the allantoic sac. These observations are contrary to what was found in this study, suggesting a different mechanism for nanoparticle clearance from the embryonic body through either passive or active means. While contrast in the allantois was significantly less than other organ systems considered immediately postinjection, the transient increase in enhancement can be due to many reasons, namely slower transport and less permeable blood vessels into the allantois resulting in a time lag for contrast enhancement of the allantois.

The use of nanoparticle based soft tissue contrast presents the questions of particle toxicity and stipulations for the use in live embryonic systems. Previous studies and literature reviews outline the known toxicity of gold nanoparticles with several metrics including MTT assays for metabolic disruption, apoptosis, and oxidative stress (Aillon et al., 2009; Jia et al., 2009; Pan et al., 2009). Some of the most influential attributes of nanoparticles that result in toxic effects to cell populations include particle size, dose, and surface charge. Pan et al found that smaller particles (<2 nm) exhibit mitochondrial damage, necrosis, and oxidative stress, whereas 15-nm gold particles did not (Pan et al., 2009). Additionally, particles less than a couple of nanometers in diameter have been shown to have chemical reactivity that is not observed with larger sized particles (Turner et al., 2008). Goodman and colleagues indicated that cationic particles display toxic effects suspected of malignant interactions with the negatively charged cellular membrane whereas the anionic counterpart to these particles were nontoxic (Goodman et al., 2004). We have

found that approximately 10% blood volume bolus injections with material concentrations as high as 300 mg/ml are nontoxic. Preliminarily, we have observed that volume injections approaching or exceeding 20% blood volume result in a nonrecoverable decrease in heart rate.

The data presented here capture static live imaging at a single stage of development; future studies and the development of new technology could address such questions as the biodistribution and residence time of particles in older stage embryos (days 4–10) with changing tissue architecture and material properties affecting the behavior of the particles. Extension of the 110-nm EXTN particles into later stage embryos will elucidate changes in material properties and extracellular environments. Differential particle movements within the tissue and changes in clearance patterns, indicative of renal system development, will give critical insights into key morphogenetic events occurring simultaneously through the entire embryo.

Furthermore, avian embryos develop in a similar manner as mammals capable of developing relevant congenital malformations through surgical manipulation or genetic perturbation (Hogers et al., 1999). Parsing out tissue contributions and changes in morphogenesis within live, diseased embryos with clinically relevant defects is paramount for quantitative 3D analysis of dysregulation during abnormal development. With the development of novel and adaptation of current technologies for mid-late stage live in vivo microCT imaging of embryonic development, our understandings and capabilities of studying this elusive stage of morphogenesis will be realized. Coupling high-resolution 3D imaging technologies with long-term tissue contrast will profoundly increase our current understanding of fundamental morphogenetic analysis.

Experimental Procedures

Preparation of Embryonic Samples and In Vivo Microinjections

White Leghorn eggs (Cornell Poultry) were incubated for 3 days at 99.5 degF and 55% humidity. After 3 days, embryos were cultured in ovo from a method previously described in (Nakamura and Funahashi, 2001). Eggs were cleaned with 70% ethanol and a small opening was created at the narrow end of the egg with the point of sterile dissection scissors. Approximately 6–7 ml of albumen was removed using a 21-gauge needle and the opening was secured with a small piece of masking tape. Two large strips of masking tape were placed down the egg and a small window was made in the egg shell using curved dissection scissors allowing visualization of the embryo. The window was covered with sterilized plastic wrap. Following in ovo culture, the embryos were housed in sterilized Styrofoam incubators maintained at appropriate temperature and humidity for proper development for the duration of the experiment.

A gravity driven pressure gradient and micromanipulator were used to microinject chick embryos as previously described by Butcher and colleagues (2007). Borosilicate capillary tubes (outside diameter, 1.00 mm; inside diameter, 0.75 mm) were drawn into microneedles and beveled at a 45 deg angle using a microforge forming needles 20 µm in diameter. Soft tissues were visualized through a dissecting light microscope and contrast media was injected through extraembryonic vessels in the vitelline network.

Contrast Media Toxicity Based on Heart Rate and Morphology

Day 3 chick embryos were injected with approximately 10% blood volume, in line with previously described literature (Henning et al., 2011). Three different nanoparticles were tested: a 110-nm alkaline earth metal particles (110-nm EXTN, Miltenyi Biotec, Inc., $n = 4$) and two gold nanoparticles (1.9-nm AuNP, 15-nm AuNP, Nanoprobes Inc., $n = 9$). The heart rate was monitored immediately before and after injection, 1 hr, and 24 hr post-injection. EBSS ($n = 9$) served as an injection sham control. At day 10 of development, the embryos were killed and fixed in 4% paraformaldehyde (PFA). Images of the embryos were taken on a stereo Zeiss microscope and anatomical measurements were analyzed in ImageJ. The WL, FL, ED, and CRL were measured in triplicate for each sample. The WL and FL were measured from the bend the limb to the furthest tip following the curvature of the limb. The eye diameter was measured across the middle of the eye with the head aligned flat with the microscope and the CRL was measured from the tip of the beak to the tail following the curvature from the ventral side of the face, following cranial to the top of the head and then caudally down the backside to the tail. All sample measurements were compared against EBSS injected controls.

In Vivo MicroCT Scanning

Day 4 ($n = 3$) nanoparticle injected embryos were taken from the portable Styrofoam incubator and placed in a custom built polycarbonate imaging chamber. All imaging was completed on a GE Healthcare eXplore CT 120 scanner. Embryos were scanned at 50 μm for 5 min with a total of 800 projections with a voltage of 80 kV. Postprocessing was completed in MicroView (GE Healthcare) for quantification of contrast levels and OsiriX (Apple) for three dimensional reconstructions. Contrast intensity gray scale values were converted to HU, correlating to bone material density (Badea et al., 2008) from calibration to a bone standard phantom with known gross densities reflective of cortical bone (SB3, GE). Contrast enhancement measurements reported reflect the attenuation within the embryo above that of the surrounding yolk and albumen attenuation.

Image Analysis and Quantification

Virtual 2D cross-sections were analyzed in MicroView using the Line Tool, measuring the contrast intensity of the heart, dorsal aorta, limb, head, and allantois. Contrast enhancement and degradation were modeled over a 24-hr period of time. DICOM image stacks were imported into OsiriX and used to produce MIPs and VRs of representative day 4 samples.

Particle perfusion quantification from the dorsal aorta immediately postinjection and 8 hr postinjection images were used for contrast enhancement measurements at known distance from the dorsal aorta. Measurements were taken parallel to the dorsal aorta at known variable distances in multiple ($n = 3$) embryos. Contrast enhancement inside the dorsal aorta at 0 hr was used as the initial concentration value based on the contrast enhancement. All measurements were normalized to the background attenuation (albumen and yolk). We approximated the flank perfusion as a radially symmetric process (emanating from the vessel wall) resulting in a 1D axi-symmetric system. Fick's First Law (Eq. 1)

was used to calculate the relative perfusion with respect to a perpendicular distance away from the dorsal aorta.

$$J = -P \frac{dC}{dX} \quad (1)$$

The flux (J) was determined through a 1-mm² area where individual contrast measurements were taken. The change in concentration (dC) with respect to the change in distance (dX) was determined based on the differences between the 8 hr postinjection image vs. the 0 hr image with the initial concentration being the amount of contrast inside the dorsal aorta and the initial distance being the wall of the aorta. The perfusion (P , reported in $\mu\text{m}^2/\text{s}$) was determined from Equation 1 with the flux (J), change in concentration (dC), and change in distance (dX) determined from the image data.

Statistics

One-way and two-way analysis of variance (ANOVA) and t -test was used to compare contrast enhancement as described in the results. Heart rate and anatomical measurements were compared with EBSS controls by means of t -test. Data are presented as a mean and standard deviation. $P < 0.05$ denoted statistical significance.

Acknowledgments

The authors acknowledge Heming Zhao for her laboratory assistance and dedication to the project. Furthermore, the authors acknowledge Mark Riccio and Dr. Fred VonStein for their technical assistance in the operation of the microCT machine and image reconstructions along with the Cornell Institute for Biotechnology. J.T.B. is funded by the National Heart, Lung, and Blood Institute, National Science Foundation, and the Hartwell Foundation. C.L.G. is funded by the National Heart, Lung, and Blood Institute and the National Science Foundation.

References

- Aillon KL, Xie Y, El-Gendy N, Berkland CJ, Forrest M.L. 2009. Effects of nanomaterial physicochemical properties on in vivo toxicity. *Adv Drug Deliv Rev* 61:457–466.
- Ashton JR, Clark DP, Moding EJ, Ghaghada K, Kirsch DG, West JL, Badea CT. 2014. Dual-energy micro-CT functional imaging of primary lung cancer in mice using gold and iodine nanoparticle contrast agents: a validation study. *PLoS One* 9:e88129.
- Badea CT, Drangova M, Holdsworth D, Johnson GA. 2008. In vivo small animal imaging using micro-CT and digital subtraction angiography. *Phys Med Biol* 53:1–36.
- Bellairs R, Osmond M. 2014. *Atlas of chick development*. Amsterdam: Elsevier.
- Boll H, Nittka S, Doyon F, Neumaier M, Marx A, Kramer M, Groden C, Brockmann MA. 2011. Micro-CT based experimental liver imaging using a nanoparticulate contrast agent: a longitudinal study in mice. *PLoS One* 6:e25692.
- Butcher JT, Sedmera D, Guldborg RE, Markwald RR. 2007. Quantitative volumetric analysis of cardiac morphogenesis assessed through micro-computed tomography. *Dev Dyn* 236:802–809.
- Cui C, Filla MB, Jones EA, Lansford R, Cheuvront T, Al-Roubaie S, Rongish BJ, Little CD. 2013. Embryogenesis of the first circulating endothelial cells. *PLoS One* 8:e60841.
- Czirók A, Rongish BJ, Little CD. 2004. Extracellular matrix dynamics during vertebrate axis formation. *Dev Biol* 268:111–122.
- Degenhardt K, Wright AC, Horng D, Padmanabhan A, Epstein JA. 2010. Rapid 3D phenotyping of cardiovascular development in mouse embryos by micro-CT with iodine staining. *Circulation. Cardiovasc Imaging* 3:314–322.

- Diaspro A, Chirico G, Collini M. 2005. Two-photon fluorescence excitation and related techniques in biological microscopy. *Q Rev Biophys* 38:97–166.
- Dickinson ME, Simbuerger E, Zimmermann B, Waters CW, Fraser SE. 2003. Multiphoton excitation spectra in biological samples. *J Biomed Opt* 8:329–338.
- Goodman CM, McCusker CD, Yilmaz T, Rotello VM. 2004. Toxicity of gold nanoparticles functionalized with cationic and anionic side chains. *Bioconj Chem* 15:897–900.
- Graves JS, Dunn BE, Brown SC. 1986. Embryonic chick allantois: functional isolation and development of sodium transport. *Am J Physiol* 251(Pt 1):C787–C794.
- Gregg CL, Butcher JT. 2012. Quantitative in vivo imaging of embryonic development: opportunities and challenges. *Differentiation* 84:149–162.
- Gregg CL, Butcher JT. 2013. Translational paradigms in scientific and clinical imaging of cardiac development. *Birth Defects Res C Embryo Today* 99:106–120.
- Gregg CL, Recknagel AK, Butcher JT. 2015. Micro/nano-computed tomography technology for quantitative dynamic, multi-scale imaging of morphogenesis. *Methods Mol Biol* 1189:47–61.
- Henning AL, Jiang MX, Yalcin HC, Butcher JT. 2011. Quantitative three-dimensional imaging of live avian embryonic morphogenesis via micro-computed tomography. *Dev Dyn* 240:1949–1957.
- Hogers B, DeRuiter MC, Gittenberger-de Groot AC, Poelmann RE. 1999. Extraembryonic venous obstructions lead to cardiovascular malformations and can be embryolethal. *Cardiovasc Res* 41:87–99.
- Jia HY, Liu Y, Zhang XJ, Han L, Du LB, Tian Q, Xu YC. 2009. Potential oxidative stress of gold nanoparticles by induced-NO releasing in serum. *J Am Chem Soc* 131:40–41.
- Johnson JT, Hansen MS, Wu I, Healy LJ, Johnson CR, Jones GM, Capocchi MR, Keller C. 2006. Virtual histology of transgenic mouse embryos for high-throughput phenotyping. *PLoS Genet* 2:e61.
- Kim JS, Min J, Recknagel AK, Riccio M, Butcher JT. 2011. Quantitative three-dimensional analysis of embryonic chick morphogenesis via microcomputed tomography. *Anat Rec* 294:1–10.
- Lee CL, Min H, Befera N, Clark D, Qi Y, Das S, Johnson GA, Badea CT, Kirsch DG. 2014. Assessing cardiac injury in mice with dual energy-microCT, 4D-microCT, and microSPECT imaging following partial-heart irradiation. *Int J Radiat Oncol Biol Phys* 88:686–693.
- Melancon MP, Zhou M, Zhang R, Xiong C, Allen P, Wen X, Huang Q, Wallace M, Myers JN, Stafford RJ, Liang D, Ellington AD, Li C. 2014. Selective uptake and imaging of aptamer- and antibody-conjugated hollow nanospheres targeted to epidermal growth factor receptors overexpressed in head and neck cancer. *ACS Nano* 8:4530–4538.
- Metscher BD. 2009. MicroCT for developmental biology: a versatile tool for high-contrast 3D imaging at histological resolutions. *Dev Dyn* 238:632–640.
- Metscher BD, Müller GB. 2011. MicroCT for molecular imaging: quantitative visualization of complete three-dimensional distributions of gene products in embryonic limbs. *Dev Dyn* 240:2301–2308.
- Nakamura H, Funahashi J. 2001. Introduction of DNA into chick embryos by in ovo electroporation. *Methods* 24:43–48.
- Nebuloni L, Kuhn GA, Müller R. 2013. A comparative analysis of water-soluble and blood-pool contrast agents for in vivo vascular imaging with micro-CT. *Acad Radiol* 20:1247–1255.
- Pan Y, Leifert A, Ruau D, Neuss S, Bornemann J, Schmid G, Brandau W, Simon U, Jahnen-Dechent W. 2009. Gold nanoparticles of diameter 1.4 nm trigger necrosis by oxidative stress and mitochondrial damage. *Small* 5:2067–2076.
- Risau W, Flamme I. 1995. Vasculogenesis. *Annu Rev Cell Dev Biol* 11:73–91.
- Roger VL, Go AS, Lloyd-Jones DM, Adams RJ, Berry JD, Brown TM, Carnethon MR, Dai S, de Simone G, Ford ES, Fox CS, Fullerton HJ, Gillespie C, Greenlund KJ, Hailpern SM, Heit JA, Ho PM, Howard VJ, Kissela BM, Kittner SJ, Lackland DT, Lichtman JH, Lisabeth LD, Makuc DM, Marcus GM, Marelli A, Matchar DB, McDermott MM, Meigs JB, Moy CS, Mozaffarian D, Mussolino ME, Nichol G, Paynter NP, Rosamond WD, Sorlie PD, Stafford RS, Turan TN, Turner MB, Wong ND, Wylie-Rosett J. 2010. Heart disease and stroke statistics—2011 update: a report from the American Heart Association. *Circulation* 123:e18–e209.
- Roy S, Hirano A, Kochen JA, Zimmerman HM. 1974. The fine structure of cerebral blood vessels in chick embryo. *Acta Neuropathol* 30:277–285.
- Sabin F. 1917. Origin and development of the primitive vessels of the chick and of the pig. *Carnegie Inst Wash* 6:64.
- Scheller B, Hennen B, Thünenkötter T, Mrowietz C, Markwirth T, Schieffer H, Jung F. 1999. Effect of X-ray contrast media on blood flow properties after coronary angiography. *Thromb Res* 96:253–260.
- Shen Y, Leatherbury L, Rosenthal J, Yu Q, Pappas MA, Wessels A, Lucas J, Siegfried B, Chatterjee B, Svenson K, Lo CW. 2005. Cardiovascular phenotyping of fetal mice by noninvasive high-frequency ultrasound facilitates recovery of ENU-induced mutations causing congenital cardiac and extracardiac defects. *Physiol Genom* 24:23–36.
- Squirrel JM, Wokosin DL, White JG, Bavister BD. 1999. Long-term two-photon fluorescence imaging of mammalian embryos without compromising viability. *Nat Biotechnol* 17:763–767.
- Supatto W, Débarre D, Moulia B, Brouzés E, Martin J-L, Farge E, Beaurepaire E. 2005. In vivo modulation of morphogenetic movements in *Drosophila* embryos with femtosecond laser pulses. *Proc Natl Acad Sci U S A* 102:1047–1052.
- Supatto W, McMahon A, Fraser SE, Stathopoulos A. 2009. Quantitative imaging of collective cell migration during *Drosophila* gastrulation: multiphoton microscopy and computational analysis. *Nat Protoc* 4:1397–1412.
- Turner M, Golovko VB, Vaughan OP, Abdulkin P, Berenguer-Murcia A, Tikhov MS, Johnson BF, Lambert RM. 2008. Selective oxidation with dioxygen by gold nanoparticle catalysts derived from 55-atom clusters. *Nature* 454:981–983.
- Wen X, Wu QP, Lu Y, Fan Z, Charnsangavej C, Wallace S, Chow D, Li C. 2001. Poly(ethylene glycol)-conjugated anti-EGF receptor antibody C225 with radiometal chelator attached to the termini of polymer chains. *Bioconj Chem* 12:545–553.
- Wessels A, Sedmera D. 2003. Developmental anatomy of the heart: a tale of mice and man. *Physiol Genom* 15:165–176.
- Yalcin HC, Shekhar A, McQuinn TC, Butcher JT. 2011. Hemodynamic patterning of the avian atrioventricular valve. *Dev Dyn* 240:23–35.
- Yu B, Mao Y, Bai L, Herman SE, Wang X, Ramanunni A, Jin Y, Mo X, Cheney C, Chan KK, Jarjoura D, Marcucci G, Lee RJ, Byrd JC, Lee LJ, Muthusamy N. 2015. Targeted nanoparticle delivery overcomes off-target immunostimulatory effects of oligonucleotides and improves therapeutic efficacy in chronic lymphocytic leukemia. *Blood* 121:136–147.
- Yu Q, Shen Y, Chatterjee B, Siegfried BH, Leatherbury L, Rosenthal J, Lucas JF, Wessels A, Spurney CF, Wu YJ, Kirby ML, Svenson K, Lo CW. 2004. ENU induced mutations causing congenital cardiovascular anomalies. *Development* 131:6211–6223.
- Zamir EA, Czirik A, Cui C, Little CD, Rongish BJ. 2006. Mesodermal cell displacements during avian gastrulation are due to both individual cell-autonomous and convective tissue movements. *Proc Natl Acad Sci U S A* 103:19806–19811.
- Zarschler K, Prapainop K, Mahon E, Rocks L, Bramini M, Kelly PM, Stephan H, Dawson KA. 2014. Diagnostic nanoparticle targeting of the EGF-receptor in complex biological conditions using single-domain antibodies. *Nanoscale* 6:6046–6056.